Mon. Not. R. Astron. Soc. **000**, 1–14 (2011) Printed 8 November 2011 (MN LATEX style file v2.2)

Optical and Infrared Imaging and Spectroscopy of the Multiple-Shell Planetary Nebula NGC 6369

G. Ramos-Larios[1⋆], M.A. Guerrero[2⋆], R. Vázquez[3⋆] and J.P. Phillips[1]†
[1] *Instituto de Astronomía y Meteorología, Av. Vallarta No. 2602, Col. Arcos Vallarta, C.P. 44130 Guadalajara, Jalisco, Mexico*
[2] *Instituto de Astrofísica de Andalucía, IAA-CSIC, C/ Glorieta de la Astronomía s/n, 18008 Granada, Spain*
[3] *Instituto de Astronomía, Universidad Nacional Autónoma de México, Apdo. Postal 877, 22800 Ensenada, B.C., Mexico*

Accepted 2011 October 25. Received 2011 October 25; in original form 2011 August 8

ABSTRACT

NGC 6369 is a double-shell planetary nebula (PN) consisting of a bright annular inner shell with faint bipolar extensions and a filamentary envelope. We have used ground- and space-based narrow-band optical and near-IR images, broad-band mid-IR images, optical long-slit echelle spectra, and mid-IR spectra to investigate its physical structure. These observations indicate that the inner shell of NGC 6369 can be described as a barrel-like structure shape with polar bubble-like protrusions, and reveal evidence for H_2 and strong polycyclic aromatic hydrocarbons (PAHs) emission from a photo-dissociative region (PDR) with molecular inclusions located outside the bright inner shell. High-resolution *HST* narrow-band images reveal an intricate excitation structure of the inner shell and a system of "cometary" knots. The knotty appearance of the envelope, the lack of kinematical evidence for shell expansion and the apparent presence of emission from ionized material outside the PDR makes us suggest that the envelope of NGC 6369 is not a real shell, but a flattened structure at its equatorial regions. We report the discovery of irregular knots and blobs of diffuse emission in low-excitation and molecular line emission that are located up to 80″ from the central star, well outside the main nebular shells. We also show that the filaments associated to the polar protrusions have spatial extents consistent with post-shock cooling regimes, and likely represent regions of interaction of these structures with surrounding material.

Key words: (ISM:) planetary nebulae: individual: NGC 6369 — ISM: jets and outflows — infrared: ISM — ISM: lines and bands

1 INTRODUCTION

The planetary nebula (PN) NGC 6369 possesses a double-shell morphology consisting of a round bright inner shell and a fainter filamentary outer shell or envelope (Schwarz, Corradi, & Melnick 1992). Its most remarkable morphological features are two disparate extensions of the inner shell along the east and west directions; the latter appears as a large, filamentary blister or *ansae*, whilst the former is a bifurcated structure.

Using low-dispersion spectroscopy, Monteiro et al. (2004) modelled the peculiar morphology of NGC 6369 as a tilted collar of gas and two symmetrically located caps of emission. This interpretation is consistent with the spheroidal shell and faint bipolar extensions proposed by Steffen & López (2006) based on a single long-slit high-dispersion spectrum obtained along the nebular major axis. These simplified models do not deal with the bifurcated structure to the eastern side of the inner shell, nor they consider the filamentary appearance of the envelope. These have been proposed to represent fast low ionisation emission regions (FLIERs, Hajian et al. 1997), although evidence for fast expansion velocities is lacking.

The H I and He II Zanstra temperatures of NGC 6369 have been reported to be T_Z(H I) ≅ T_Z(He II) ≅ 70,000 K (e.g., Phillips 2003), comparable to estimates deriving from the energy balance method (Pottasch & Bernard-Salas 2008). The similarity of the H I and He II Zanstra temperatures suggests that the nebula is optically thick to H ionizing radiation, and thus that significant amounts of molecular material and dust may be present outside the ionisation bound optical nebula. This is consistent with the *ISO* (Infrared Space Observatory) indications of emission from polycyclic aromatic hydrocarbons (PAHs) bands

⋆ E-mail: gerardo@astro.iam.udg.mx (GRL); mar@iaa.es (MAG); vazquez@astro.unam.mx (RV)
† Deceased, April 29th, 2011

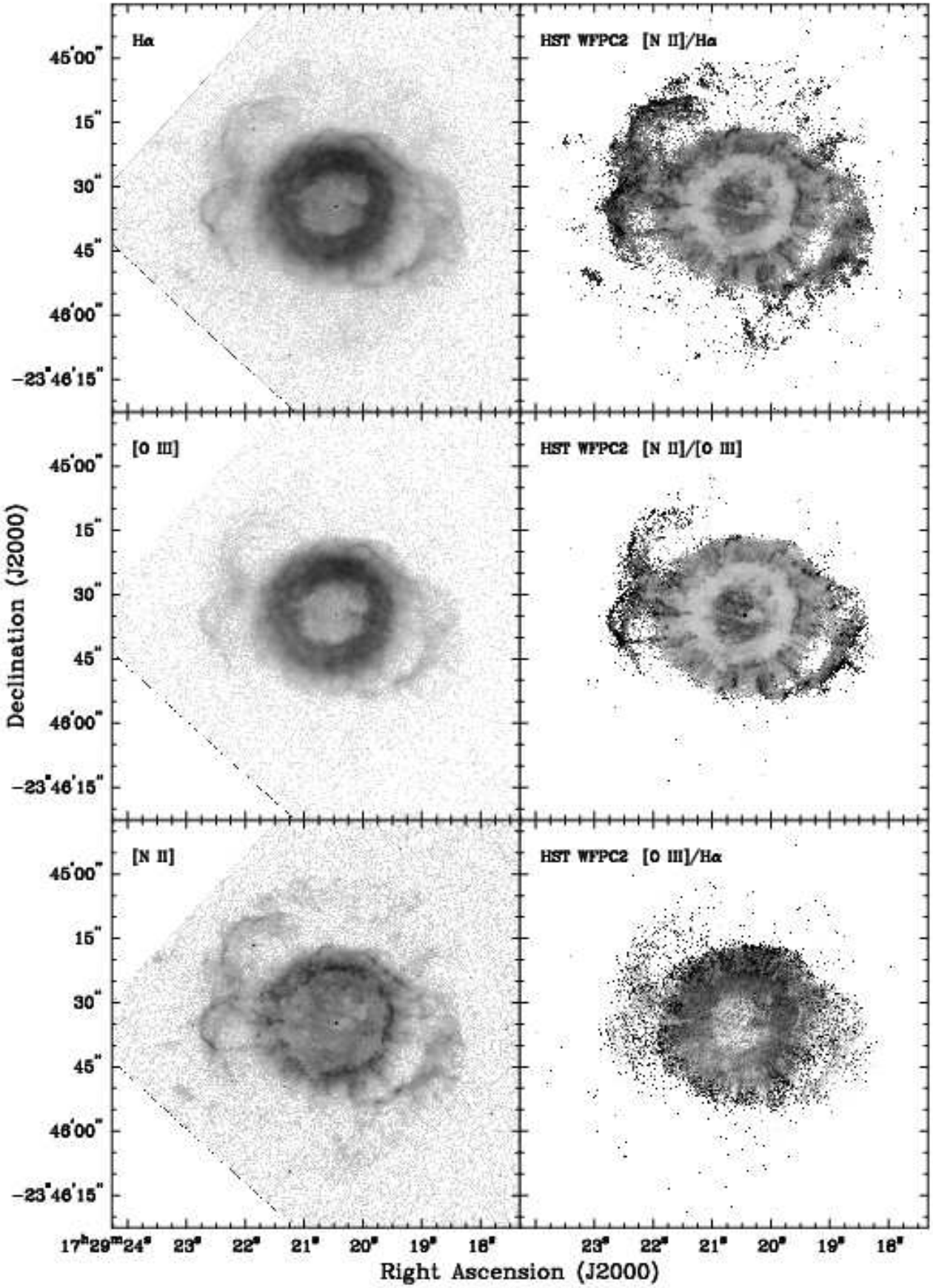

Figure 1. (*left panels*) *HST* WFPC2-WF3 images of the inner shell of NGC 6369 in the Hα, [O III] λ5007, and [N II] λ6583 emission lines, and (*right panels*) [N II]/Hα, [N II]/[O III], and [O III]/Hα ratio maps.

(Cohen & Barlow 2005) that would be produced at a photodissociation region (PDR) located outside of the ionized shell. There is also evidence of dust emission from NGC 6369. *ISO* spectroscopic observations of NGC 6369 have showed it to be one of the few evolved PNe to possess the 21 and 30 μm emission features (Hony, Waters, & Tielens 2001) that are typically observed in C-rich AGB stars and PNe (e.g., Kwok, Volk, & Hrivnak 1999; Van Winckel & Reyniers 2000; Hrivnak, Volk, & Kwok 2009). The origin of these spectral features is unclear, although it has been suggested that the 21 μm emission may arise from an extraordinarily wide range of agents, including hydrogenated fullerenes, nanodiamonds, SiC+SiO_2 grains, and TiC nanoclusters (see e.g., Zhang, Jiang, & Li 2009, and references therein). The carbon dust origin in NGC 6369 is consistent with its high C/O ratio, $\sim$2 (Zuckerman & Aller 1986; Aller & Keyes 1987).

In order to investigate the kinematics and three-dimensional structure of the main nebula and envelope of NGC 6369 and to confirm the occurrence of an outer envelope of molecular material, we have acquired new narrow-band near-IR H_2 and optical images, and long slit high-dispersion spectroscopic observations that have been examined in conjunction with archival mid-IR *ISO* spectra and *Spitzer* images and spectra, as well as optical narrow-band *HST* images. The observations and archival data are presented in §2, and the results on the morphology, and mid-IR spectroscopy are described in §3, and §4, respectively. The kinematics and the discussion are presented in §5 and final conclusions are presented in §6.

2 OBSERVATIONS

2.1 Optical imaging

Narrow-band images in the [N II], Hα, and [O III] emission lines were obtained on September 1, 2008 using ALFOSC (Andalucia Faint Object Spectrograph and Camera) at the 2.56-m Nordic Optical Telescope (*NOT*) in the Observatorio de Roque de los Muchachos (ORM, La Palma, Spain). The detector was a 2048×2048 EEV CCD with plate scale 0.″19 arcsec pix^{-1}, resulting in a field of view (FoV) of 6.′5×6.′5. The central wavelengths and bandwidths of the filters are λ_c=6589 Å and $\Delta\lambda$=9 Å for [N II], λ_c=6568 Å and $\Delta\lambda$=8 Å for Hα, and λ_c=5007 Å and $\Delta\lambda$=8 Å for [O III]. The spatial resolution achieved during the observations, as determined from the FWHM of stars in the FoV, was 0.″95. Either two or three individual frames with integration times of 300 s were taken for each filter, leading to total exposure times of 900 s for the [N II] image, and 600 s for the Hα and [O III] images. The data were bias-subtracted and flat-fielded with twilight flats using standard IRAF[1] routines.

Narrow-band *HST* WFPC2 images of NGC 6369 in the [N II] λ6583, Hα, and [O III] λ5007 emission lines were retrieved from MAST, the Multimission Archive at the Space Telescope Science Institute[2] (Prop. ID: 9582, Hubble Heritage Observations of NGC 6369, PI: Keith Noll). The nebula was registered by the WF3 detector with a pixel scale of 0.″09. Four individual exposures were obtained using the F658N (pivot wavelength λ_p=6590.8 Å, $\Delta\lambda$=28.5 Å), F656N (λ_p=6563.8 Å, $\Delta\lambda$=21.5 Å), and F502N (λ_p=5012.4 Å, $\Delta\lambda$=26.9 Å) filters, resulting in total exposure times of 1,040 s for the [N II] λ6583 image, and 640 s for the Hα and [O III] λ5007 images (Figure 1).

2.2 Near-IR imaging

Narrow-band H_2, Brγ and continuum K_c near-IR images of NGC 6369 were obtained on 2010 June 27 using LIRIS, the Long-Slit Intermediate Resolution Infrared Spectrograph (Acosta-Pulido et al. 2003), at the Cassegrain focus of the 4.2-m William Herschel Telescope (*WHT*) on Roque de Los Muchachos Observatory (ORM, La Palma, Spain). The detector was a 1k×1k HAWAII array sensitive in the spectral range from 0.8 to 2.5 μm. The plate scale is 0.″25 pix^{-1} and the FoV 4.′27×4.′27. The narrow-band filters have λ_c=2.1218 μm and $\Delta\lambda$=0.032 μm for H_2 (1−0) S(1), λ_c=2.1658 μm and $\Delta\lambda$=0.032 μm for Brγ, and λ_c=2.270 μm and $\Delta\lambda$=0.034 μm for K_c.

Ten 60 s exposures were taken for each filter, for total effective exposure times of 600 s. The jitter option was used to increase the sampling of the sky: the telescope pointing of each exposure is shifted by a few pixels, thus rastering the nebula to different locations on the detector. Each series of observations on the object was followed by similar series of observations on adjacent blank sky positions. The reduction of the LIRIS data was carried out using the dedicated software LIRISDR (LIRIS Data Reduction package), a pipeline for the automatic reduction of near-IR data developed within the IRAF environment. The reduction performed by LIRISDR includes standard and additional non-standard steps such as bad pixel mapping, cross-talk correction, flat-fielding, sky subtraction, removal of reset anomaly effect, field distortion correction, and final image co-addition. The continuum contribution to the H_2 and Brγ emission was subsequently removed using the K_c image. In this process, we did not find necessary to scale the images since the H_2, Brγ, and K_c filters have very similar bandwidths and transmissions. The spatial resolution on the WHT images, as determined from the FWHM of stars in the field of view, is $\sim$0.″8. The narrow-band continuum-subtracted H_2 and Brγ images of NGC 6369 are presented in Figure 2.

2.3 Mid-IR imaging

Spitzer Infrared Array Camera (IRAC; Fazio et al. 2004) images of NGC 6369 (Figure 3) were retrieved from the NASA/IPAC Infrared Science Archive (IRSA). The images, obtained on 2005 September 22 as part of Program 20119 (The Darkest Cloud, An IRAC/MIPS Survey of the Pipe Nebula, PI: C.J. Lada), have been processed as described

[1] IRAF, the Image Reduction and Analysis Facility, is distributed by the National Optical Astronomy Observatory, which is operated by the Association of Universities for Research in Astronomy (AURA) under cooperative agreement with the National Science Foundation.

[2] STScI is operated by the Association of Universities for Research in Astronomy, Inc., under NASA contract NAS5-26555.

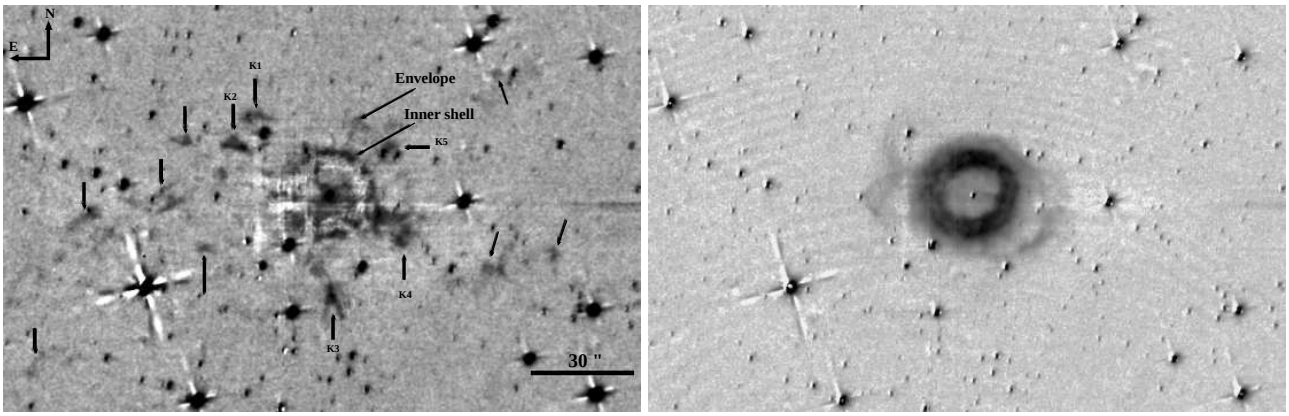

Figure 2. WHT LIRIS H_2 (*left*) and Brγ (*right*) background-subtracted images of NGC 6369. The dark and light diffraction spikes are a result of the rotation of the focal reducer during the acquisition of the images. The envelope and inner shell are labeled. The arrows point to knots and blobs of diffuse H_2 emission. In the envelope, five knots, marked as knots K1 to K5, have been highlighted.

in the IRAC data handbook[3]. The observations employed filters having isophotal wavelengths (and bandwidths $\Delta\lambda$) of 3.550 μm ($\Delta\lambda$=0.75 μm), 4.493 μm ($\Delta\lambda$=1.9015 μm), 5.731 μm ($\Delta\lambda$ = 1.425 μm), and 7.872 μm ($\Delta\lambda$ = 2.905 μm). IRAC spatial resolution varies between $\simeq$1.″7 and $\simeq$2.″0 (Fazio et al. 2004), and is reasonably similar in all IRAC bands, although the diffraction halo at 8 μm is stronger than at the other bands.

2.4 Long-slit high-dispersion optical spectroscopy

Long-slit high dispersion optical spectroscopy of NGC 6369 was obtained on July 17-19 2008 using the Manchester Echelle Spectrometer (MES, Meaburn et al. 2003) mounted on the 2.1 m (f/7.5) telescope at the Observatorio Astronómico Nacional de San Pedro Mártir (OAN-SPM, Mexico). A 1k×1k SITe CCD was used as detector with a 2×2 on-chip binning, resulting on a plate scale of 0.″6 pix^{-1} and a dispersion of 0.1 Å pix^{-1}. Since MES has no cross dispersion, a $\Delta\lambda$=90 Å bandwidth filter was used to isolate the 87$^{\rm th}$ order covering the spectral range which includes the Hα and [N II] λ6583 lines. At this spectral order, the slit width of 150-μm (2″) that was set during the observations corresponds to a spectral resolution of $\simeq$ 12 km s^{-1}.

Five long-slit spectra, labeled from 1 to 5 on Figure 4, were obtained to map the kinematics at different regions of the nebula. The position angles (PAs) for slits 1 to 5 are +74°, +80°, −22°, +22°, and −86°, respectively. The exposure time was 1,200 s for the spectrum at PA=+80° (slit # 2) and 1,800 s for the rest. The seeing during the observations, as determined from the FWHM of stars in the FoV, varied from 1.″2 to 2.″0. The spectra were wavelength calibrated with a Th-Ar arc lamp to an accuracy of ±1 km s^{-1}.

2.5 Mid-IR spectroscopy

Spitzer Infrared Spectrograph (IRS; Houck et al. 2004) mid-IR spectroscopic observations of NGC 6369 obtained through the *Spitzer* Program 40115 (Dual Dust Chemistry in Wolf-Rayet Planetary Nebulae, PI: G. Fazio) were retrieved from IRSA. The observations consisted of short (5.1-8.5 μm) and long (7.4-14.2 μm) wavelength spectra taken with the *Spitzer* IRS Short-Low module 2 (SL2) and 1 (SL1), respectively. Both modules have rectangular apertures $\sim$3.″6×57″ that, for these particular observations, were oriented along PA=177.18°. The observations were acquired at closely similar positions α(J2000.0)=17$^{\rm h}$ 29$^{\rm m}$ 20.$^{\rm s}$37 and δ(J2000.0)=–23° 45′ 24.″55 (positions A & C), and α(J2000.0)=17$^{\rm h}$ 29$^{\rm m}$ 20.$^{\rm s}$44 and δ(J2000.0)=–23° 45′ 43.″55 (positions B & D), resulting in overlapping slits covering the nebula along its minor axis. The spectral resolution of the observations, $\lambda/\Delta\lambda$, varied between 64 and 128. The *Spitzer* SL1 & SL2 spectra of the source are illustrated in Figure 9, where we show the results for overlapping apertures across the centre of the source (labelled A to D). All positions cover the inner shell, but positions A and C map the north portion of the envelope and positions B and D the south portion.

Similarly, we made use of mid-IR *ISO*[4] Short Wave Spectrometer (SWS; de Graauw et al. 1996) spectroscopic observations of NGC 6369 acquired on 1997 February 14 as part of program 45601901 (PI: S. Górny). *ISO* SWS provides spectra in the short (2.38-12.1 μm), medium (12-29 μm), and long (29-45.3 μm) wavelength ranges, acquired through apertures with sizes 14″×20″, 14″×27″, and 20″×22″, respectively. The *ISO* SWS spectra have an exposure time of 1,140 s, and were centred on α(J2000.0)=17$^{\rm h}$ 29$^{\rm m}$ 20.$^{\rm s}$78 and δ(J2000.0)=–23° 45′ 32.″1.

3 MORPHOLOGY

An inspection of the optical and infrared images of NGC 6369 (Figures 1, 2 and 3) confirms the three morphological components previously described in the main nebula: a bright inner shell, two extensions, and an envelope. Faint

[3] http://ssc.spitzer.caltech.edu/irac/dh/iracdata_handbook_3.0.pdf.

[4] Based on observations with ISO, an ESA project with instruments funded by ESA Member States (especially the PI countries: France, Germany, the Netherlands and the United Kingdom) and with the participation of ISAS and NASA

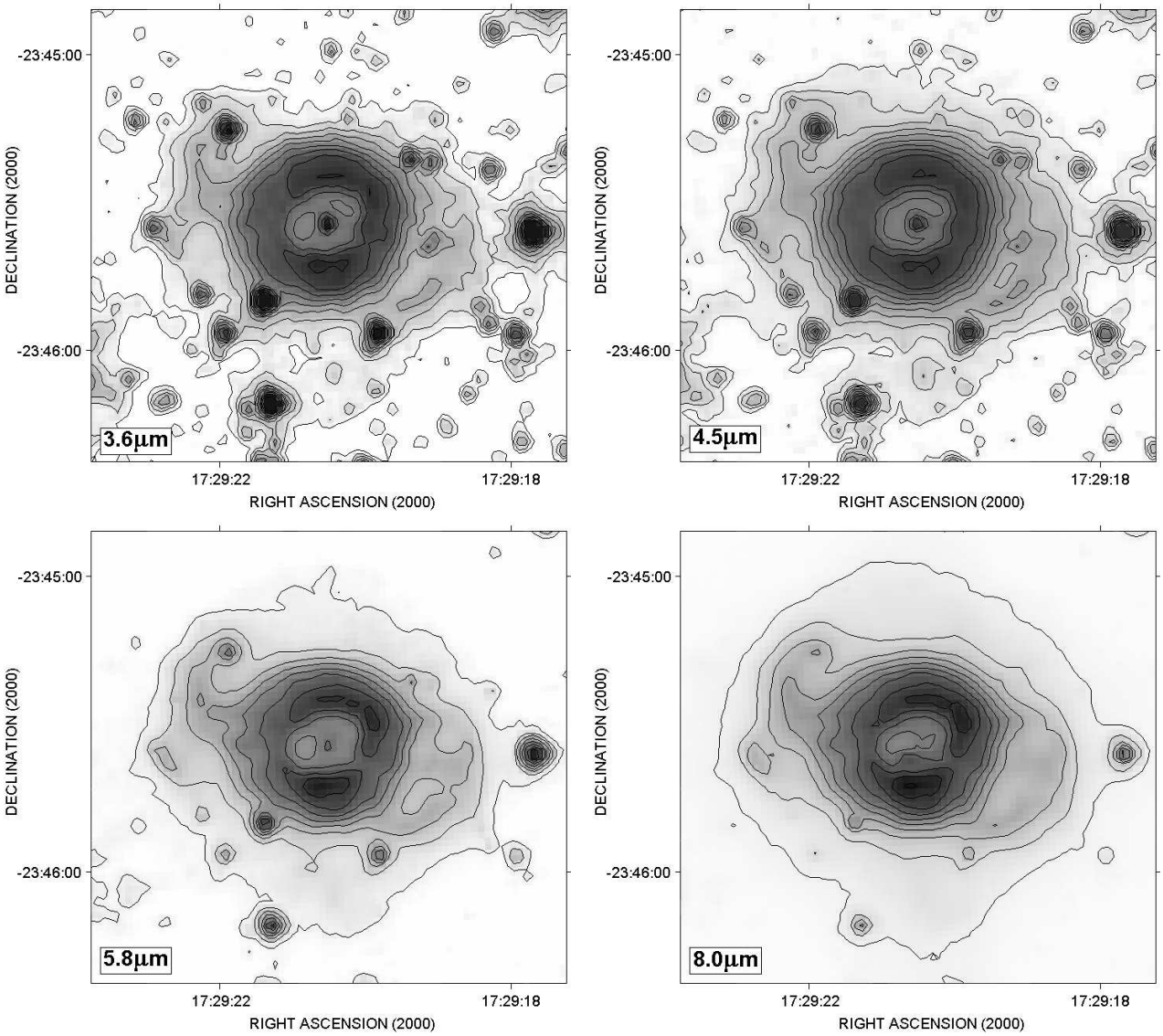

Figure 3. *Spitzer* IRAC images of NGC 6369 overplotted by contours. The contours correspond to levels of the intrinsic surface brightness, SB, defined by SB_n=A$\times 10^{(n-1)\,C} - B$ MJy sr^{-1}, where n is the contour level (n=1 corresponds to the lowest and outermost level), B is the background level, and A and C are scale parameters. The contour parameters [A, B, C] are given by (1.6, 1.018, 0.199) at 3.6 μm, (1.45, 0.792, 0.196) at 4.5 μm, (7.3, 5.264, 0.17) at 5.8 μm, and (20.5, 15.341, 0.173) at 8.0 μm. We note that the blob of diffuse emission in the 8 μm image inside the inner shell is an artifact, an echo of the brightest region of the rim.

blobs of diffuse emission are also detected outside the main nebular shells. Next we describe in detail the morphology of the main nebular shell and this newly detected extended emission.

3.1 The main nebula

3.1.1 Optical morphology

The *HST* WF3 Hα and [O III] images of the inner shell and envelope of NGC 6369 presented in Figure 1 show a thick ($\sim$5.″5) annular shell with inner radius $\simeq$8.″3. The surface brightness is noticeably uneven, with patches of bright and diminished emission. Several dark knots and lanes, reminiscent of those seen in other PNe (e.g., IC 4406 and NGC 6720, O'Dell et al. 2002) are also detectable.

The [N II] image reveals a dramatically different view of the inner shell, with the Hα and [O III] dark knots and lanes turning into bright [N II] spots and filaments, and an intricate system of [N II] filaments filling the innermost regions of the shell. Radial filaments emanate outwards from most of the [N II] knots, which are thus revealed as "tadpole" or "cometary" features very similar to those seen, e.g., in NGC 2392 (O'Dell et al. 2002) and NGC 7354 (Contreras et al. 2010). Interestingly, there is a bright ring of these cometary knots, at the location of the outer rim of the bright Hα and [O III] shells at a distance of $\simeq$12.″4 of the central star, whose tails extend at least up to $\sim$20″.

The ratio maps in Fig. 1 reveal that the bright rim has

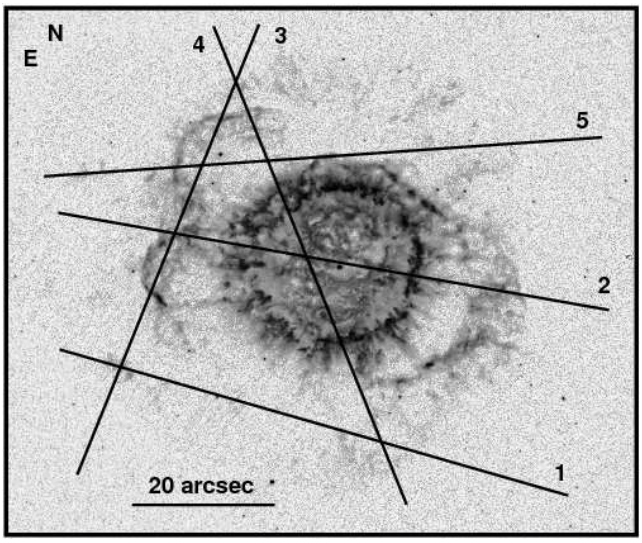

Figure 4. Slits positions used in the long-slit echelle spectroscopy of NGC 6369 superimposed upon the *HST* WFPC2-WF3 [N II] image.

high excitation, with the lowest [N II]/Hα and [N II]/[O III] values at radial distances $8''-12''$, but the regions within this shell, closer to the central star, have anomalously low ionization. At the location of the ring of knots, at $\simeq 12\farcs4$ from the central star, the "cometary" features are highlighted in the [N II]/Hα and [O III]/Hα ratio maps (Fig. 1), showing high ratio values in the former and low ratio values in the latter. The tails of these knots define an annular region with outer radius $\sim 18''$.

The peculiar extensions of the inner shell of NGC 6369 (Schwarz, Corradi, & Melnick 1992) along PA$\simeq 63^\circ$ are best seen in the Hα and [N II] images. The western extension is reminiscent of a lobe or a large *"ansa"*, whilst the eastern one displays a complex morphology best described as a bifurcated structure. The ratio maps indicate that these features have low excitation, with values of [N II]/[O III] up to 20 times larger than those in the higher excitation regions of the inner shell, and up to twice those of the ring of knots at the rim of the inner shell.

The envelope is barely detected in [O III], and only a little brighter in Hα. The [N II] emission is brighter and reveals it to be composed of an ensemble of knots, blobs, and filaments. The appearance of these knots and their tails is less defined than those in the inner shell. Overall, the emission is mostly distributed within a fragmentary annular region with inner and outer radii $25''-34''$, as illustrated by the NOT composite-colour picture of NGC 6369 presented in Figure 5-*left*.

3.1.2 Near-infrared morphology

The morphology of the bright inner shell and envelope of NGC 6369 in the near-IR Brγ line is similar to that in Hα (Fig. 2-*right*). The lack of differential extinction between the optical and near-IR lines of H I suggests little dust content in the nebula along the line of sight. By contrast, the image in the near-IR H_2 line (Fig. 2-*left*) offers a very different view of the main shell of NGC 6369. The region interior to the bright inner shell, which showed anomalously low excitation emission, is revealed to be filled with H_2 emission. This region is then encompassed by two concentric annular regions, the first one where the H_2 emission is very low, and the second one, with radius $\sim 13''$, where we find bright H_2 emission. The interior annulus is coincident with regions of high excitation in the [N II]/Hα and [N II]/[O III] ratio maps, whilst the exterior, H_2-bright annulus is coincident with the rim of the inner shell defined by the heads of the [N II] "cometary" knots. This provides evidence that the [N II] knots and filaments are associated with H_2 emission, i.e., they include significant amounts of neutral material.

The extensions of the inner shell are not detected in H_2, but the northwest quadrant of the envelope and some bright knots exhibit H_2 emission. Surprisingly, the radius of the northwest arc detected in H_2 is $\sim 25''$, i.e., this H_2 emission is interior to the annulus of [N II] emission in the envelope. As for the H_2 knots, some (e.g., K3 and K5) have easily identifiable [N II] counterparts, while for some others (e.g., K2 and K4) the identification is hampered by their spatial coincidence with the [N II]-bright eastern and western extensions of the main shell. Among the H_2 knots detected in the envelope, the morphology of knots K2 and K3 is quite noticeable, with a bright head and two tails pointing outwards from the central star.

3.1.3 Mid-infrared morphology

The mid-IR morphology of NGC 6369 is illustrated by the "unsharp" *Spitzer* IRAC colour-composite picture presented in Figure 5-*right*. In this picture, the bright optical shell is the brightest feature, whereas the outer envelope and east and west extensions are fainter but still noticeable. Despite the reduced spatial resolution, the mid-IR morphology of NGC 6369 is consistent with that observed in the *HST* (Fig. 1) and NOT (Fig 5-*left*) optical images. The reddening of the eastern and western extension of the main shell and outer envelope in this colour-composite IRAC picture implies a higher relative contribution of 8.0 μm emission at these morphological components. This is further evidenced by the contours in Figure 3; the inner ring is intense in all of the IRAC images, whereas the surface brightness of the envelope becomes relatively brighter at longer wavelengths, in the 5.8 and 8.0 μm bands.

The mid-IR surface-brightness profiles extracted from background-corrected IRAC images through the minor and major axes of the nebula (Figure 6) confirm this result. The shape of the surface brightness profile interior to the bright main shell is similar in all of the channels, with flux increasing with wavelength. By contrast, the 3.6 and 4.5 μm surface brightness profiles fall-off sharply at $\sim 25''$, whereas the emission at 5.8 and 8.0 μm show broad skirts up to $\sim 70''$. This becomes in a sharp increase of the 5.8μm/4.5μm and 8.0μm/4.5μm ratios at radial distances greater than $20''$ (Fig. 6). We also note that the 5.8μm/4.5μm and 8.0μm/4.5μm ratios take minimum values at a radial distance $\sim 15''$, i.e., the position of the bright [N II] and H_2 ring.

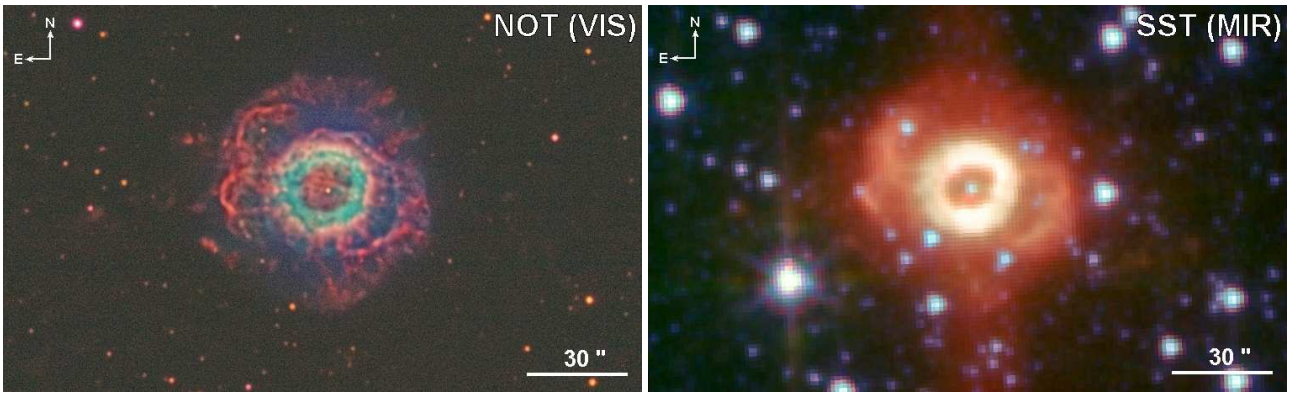

Figure 5. (*left*) Colour-composite NOT [O III] (blue), Hα (green), and [N II] (red), and (*right*) *Spitzer* IRAC 4.5 μm (blue), 5.8 μm (green), and 8.0 μm (red) pictures of NGC 6369. We note that the stretch of the NOT optical images has been chosen to highlight the faint emission from the knots and condensations outside the ionised nebular shell. We also note that the north-south band of 8.0 μm emission is an instrumental artifact.

3.2 The extended emission

The *HST* WF3 images (Fig. 1) hint the presence of irregular condensations outside the envelope of NGC 6369, towards the east and close to the edge of the WF3 FoV. The NOT [N II] image (Figure 5-*left*), which covers a greater FoV than the *HST* images, and very especially the WHT H_2 image (Figure. 2-*left*) reveal patches of diffuse emission and blobs, as marked by arrows in the H_2 image, well beyond the main ionised nebula, up to $\sim$70$''$ from the central star in [N II] and $\sim$80$''$ in H_2. These [N II] and H_2 blobs are distributed irregularly, mostly along the east-west direction, with some hints of point-symmetry. These blobs are also detected in the *Spitzer* IRAC 8 μm image (Figure 5-*right*), especially those that are well beyond the 8 μm bright envelope.

4 MID-IR SPECTROSCOPY

The *ISO* spectrum of NGC 6369 in the 2.4–4.1 μm spectral range shown in Figure 8 reveals the prevalence of emission lines, with Brα being the most intense and relatively weak or negligible emission of the 3.3 μm PAH band. There is also evidence for the H_2 1$-$0 Q(3) λ2.424 μm and H_2 1$-$0 Q(7) λ2.500 μm lines, which is consistent with the detection of H_2 emission in our WHT LIRIS images and at 17.036 μm (Pottasch & Bernard-Salas 2008). Although the spectrum remains relatively noisy, and some possible transitions are unidentified, we see evidence for Pfδ and Pfγ, as well as a couple of Humphrey transitions.

The longer wavelength *ISO* spectra are relatively noisy, precluding reliable analysis in the range $\Delta\lambda$ $\sim$4.1–10 μm, although the enhancements in emission at 6.2 and 7.8 μm suggests that PAH band features are present. The *Spitzer* IRS spectra (Figure 9) show more convincing evidence for these PAH components. The shorter wavelength SL2 spectrum (Fig. 9-*left*) shows evidence for the H_2 0$-$0 S(7) λ5.511 μm line, but the spectrum is, otherwise, dominated by four PAH bands at 6.2, 6.9, 7.8, and 8.6 μm, and an underlying continuum which raises towards longer wavelengths and that can be attributable to cool dust emission.

The same situation applies at longer wavelengths as well (Fig. 9-*right*), where the flux is dominated by PAH band emission yet again, with features at 7.8, 8.6, 11.3, 12.7 and 14.2 μm contributing a significant fraction of the total emission. We also see evidence for strong transitions due to the [Ar III] λ8.991 μm and [S IV] λ10.51 μm lines, and the possible contribution of the Huα λ12.372 μm line.

One final point is related to the relative intensities of the PAH bands themselves. The 7.8 μm feature arises primarily through C-C stretching modes, whilst the 11.3 μm band is a consequence of C-H out-of-plane bending modes. This would normally lead to I(7.8μm)/I(11.3μm)$\approx$1.3 for neutral PAHs, but radiation fields in PNe are capable of appreciably ionising the PAH molecules, reducing the strength of the 11.3 μm feature and leading to I(7.8μm)/I(11.3μm)$\approx$12 for fully ionised PAHs (Li & Draine 2001). It is thus puzzling that the I(7.8μm)/I(11.3μm) ratio appears significantly less than unity (Fig. 9-*right*) at any location of the nebula.

4.1 Interpreting the mid-IR images of NGC 6369

The mid-IR spectroscopy of NGC 6369 described above allows us to discuss the nature of the emission detected in the IRAC bands. The *ISO* data show convincingly that the emission in the IRAC 3.6 and 4.5 μm bands is largely dominated by H I lines, with the Brα λ4.052 μm line in the 4.5 μm IRAC band being the brightest line. The contribution to these bands from Bremsstrahlung and the 3.3 μm PAH band is very small or negligible. The contribution from other ionic lines in the 4.1-5.1 μm spectral range (e.g., [Mg IV] λ4.486 μm, [Ar VI] λ4.529 μm, and [K III] λ4.618 μm, Bernard Salas et al. 2001) is also possible, but the *ISO* spectrum has too low S/N and the *Spitzer* IRS SL2 spectrum missed this spectral range. Meanwhile, the emission in the 5.8 and 8.0 μm IRAC channels is dominated by the 6.2, 6.9, 7.8, and 8.6 μm PAH bands, the [Ar III] λ8.991 μm emission line, and an underlying continuum from cool dust which raises towards longer wavelengths.

The close resemblance between the images and surface brightness profiles in the 3.6 and 4.5 μm IRAC channels is due to the prominence of ionic and H I transitions in these two bands. The higher relative emission in the 5.8 and 8 μm bands at large radial distances implies that molecular material and cool dust, responsible of PAH bands and con-

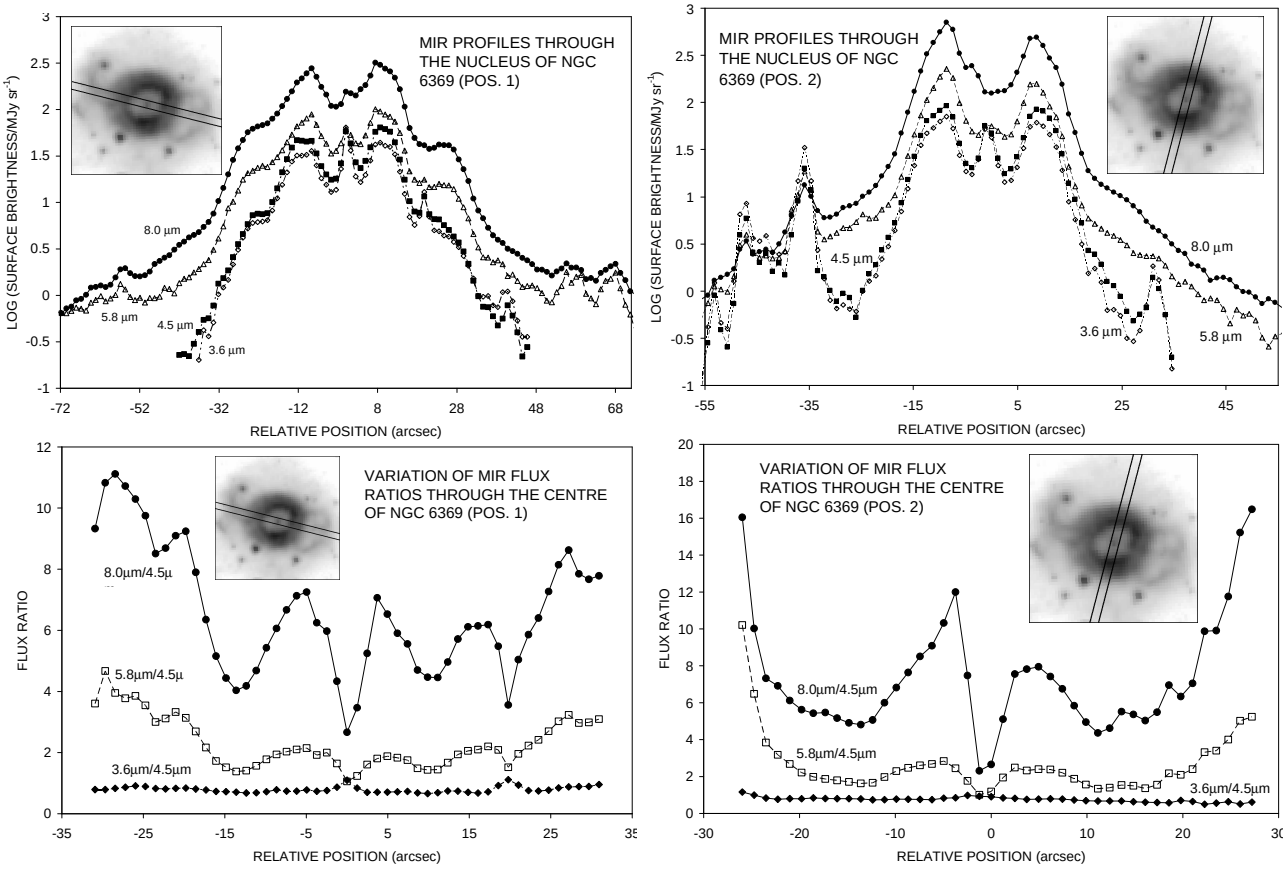

Figure 6. MIR IRAC profiles of NGC 6369 along approximate E-W (*left*) and N-S (*right*) axes through its central star as indicated in the inserted images. The lower panel shows flux ratios for the central region of the source, where 4.5 μm emission has a reasonably high S/N.

tinuum emission, are important at the eastern and western extensions of the inner shell and at the envelope, whilst ionic lines dominates the emission from the bright inner shell. The relative increase of 5.8 and 8.0 μm, [N II], and H_2 emission at the interior of the bright inner shell most likely reveal an opening of the inner shell at its polar caps, so that the emission detected at this region comes from regions far from the nebular center, above and below the bright inner shell.

Finally, we noted in §3.2 that the blobs and knots of diffuse emission outside the main nebular shells are detected in the optical [N II], near-IR H_2, and IRAC 8 μm images. Since these blobs present both emission from ionised (N^+) and molecular (H_2) material, and the IRAC 8 μm band of the main nebula is dominated by PAH bands and dust continuum, the origin of the emission in the IRAC 8 μm band may be multi-fold. The [Ar III] λ8.991 μm line is the brightest ionic line in this band, but the ionization potential of Ar^+ (IP=27.6 eV) is higher than this of N (IP=14.5 eV) and thus Ar^{++} may be not present in these regions. Indeed, the lack of [O III] emission, whose IP(O^+) is 35.1 eV, indicates that only low-excitation species are present in these regions. Since no emission from these blobs is detected in the IRAC 5.8 μm image, it seems unlikely that PAH bands or dust continuum produce the emission detected in the IRAC 8 μm image, although we concede that the levels of dust continuum and PAH emission in the IRAC 5.8 μm may be lower than in the IRAC 8 μm band. Given the previous difficulties for ionic, PAH or continuum emission and that near-IR H_2 1−0 S(1) emission is detected, we favor the H_2 0−0 S(4) λ8.0251 μm emission line as the responsible for the emission from these blobs in the IRAC 8 μm image.

5 DISCUSSION

5.1 Spatio-kinematical modelling of the inner shell of NGC 6369

Figure 7 displays the individual Hα and [N II] position-velocity (PV) maps of NGC 6369 obtained from the five slits positions illustrated in Fig. 4. Overall, the Hα and [N II] lines show similar kinematical features, but these are best seen in [N II] given that its thermal broadening is smaller than that of the Hα line. The radial velocity of the source with respect to the Local Standard of Rest was determined to have a value $V_{\rm LSR} = -89.5 \pm 1.0\,{\rm km\,s^{-1}}$, based on the mean expansion velocity at the position of the central star. This result is in excellent agreement with the value of $V_{\rm LSR} \simeq -90 \pm 6.5\,{\rm km\,s^{-1}}$ reported by Schneider et al. (1983).

The line shapes of the echellogram at slit position #2, which cuts the nebula along the east and west extensions, is closely similar to that presented by Steffen & López (2006): the east and west extensions are detected as red- and blue-

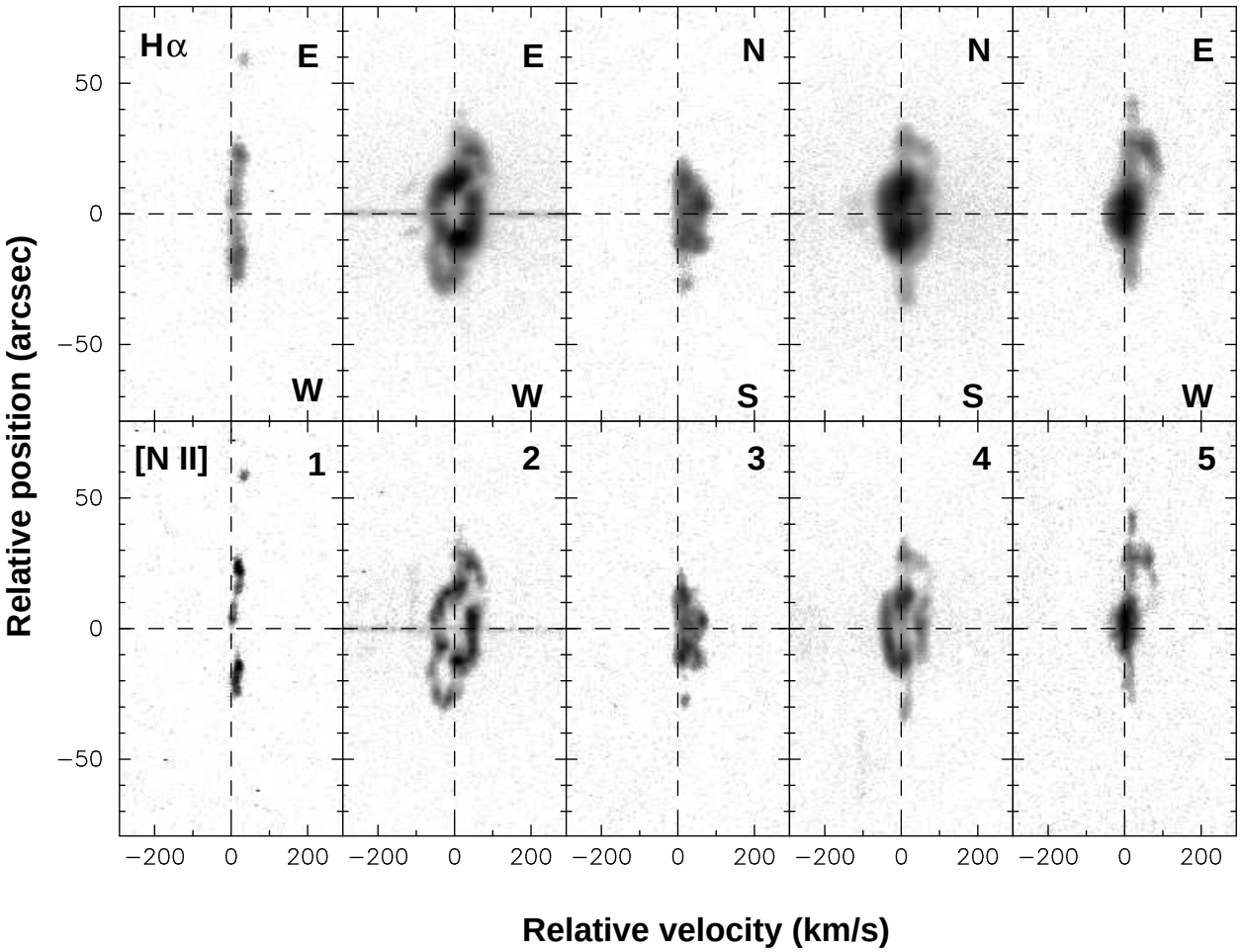

Figure 7. (*top*) Hα and (*bottom*) [N II] λ6583 position-velocity (PV) maps of NGC 6369 for slits positions #1 to #5. The slit orientation is labeled on the upper panels. The relative position is measured with respect to the horizontal dashed lines that mark the midpoint of the most intense central emission for slits #1, #3, #4, and #5, and the central star for slit #2. The vertical dashed lines correspond to the systemic radial velocity ($V_{\rm LSR} = -89.5 \pm 1\,{\rm km\,s^{-1}}$).

shifted loops, respectively, and their shape is typical of the emission in bipolar outflows. The structure of the Hα line may give the false impression that the inner shell is a closed ellipsoid, but the sharper view offered by the [N II] line reveals that the loops of the east and west extensions emanate from gaps at the tips of the inner shell.

The eastern extension is mapped in more detail by the slits at positions #3, #4, and #5. In the echellograms at positions #4 and #5, this extension is detected as a red-shifted loop, as expected for a blister-like structure. However, the echellogram at position #2 reveals a waist and two open loops that are indicative of a more complex structure.

Previous three-dimensional modeling of NGC 6369 (Monteiro et al. 2004; Steffen & López 2006) concur that this nebula has a bipolar structure, although the details make them differ significantly. Monteiro et al. (2004) obtained spatially-resolved information of the physical conditions within the nebula that, in conjunction with a photoionization model, allowed them to synthesize narrow-band images. In order to match the morphology observed in several emission lines, they adopted for NGC 6369 a clumpy hourglass structure with a thick equatorial belt and two symmetrically located caps of emission whose orientation is tilted by 30° from the symmetry axis of the main nebula. On the other hand, Steffen & López (2006) used a single high-dispersion long-slit spectrum of NGC 6369 obtained along its major axis to illustrate the capabilities of *"SHAPE"*, an interactive 3-D modeling tool. Using a Hubble-type ($v \propto r$) expansion law for NGC 6369, as it is typically assumed in PNe (e.g., Solf & Ulrich 1985; Guerrero, Manchado, & Serra-Ricart 1996; Sabbadin et al. 2000; Corradi 2004), they concluded that there is no equatorial waist in NGC 6369, but its three-dimensional structure can rather be described by a partial spheroidal shell with opened tips at its major axis from where two fainter blisters protrude as the east end west extensions.

Our more detailed spatial coverage of the kinematics of NGC 6369 allows us to refine Steffen & López (2006)'s model and to investigate the spatio-kinematical structure of the nebular envelope. Using the latest version of the code *SHAPE* (version 10; Steffen et al. 2011), we have constructed a spatio-kinematical model for NGC 6369 which fits its narrow-band images and PV maps. The quality of the fit can be judged in Figure 10 that presents a comparison between the synthetic morphology and kinematics from the model and those observed in NGC 6369. The synthetic im-

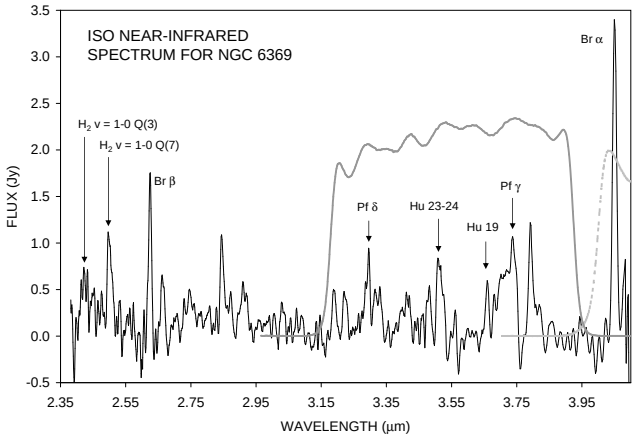

Figure 8. *ISO* spectrum of NGC 6369 extending between 2.4 and 4.1 μm, together with the ranges corresponding to the 3.6 μm (solid profile) and 4.5 μm (dashed profile) *Spitzer* IRAC channels.

age of NGC 6369 (right image of the upper panel in Fig. 10) is well matched with its *HST* Hα image (left image). Similarly, the kinematics of NGC 6369 are fairly reproduced as shown in the lower panel of Fig. 10 which presents the PV for slits #2 to #5 accompanied by the corresponding PV map extracted from the model. Our best fit model, illustrated in Figure 11, is composed of:

• an equatorial barrel with expansion velocity $\simeq$55 km s^{-1} and whose axis of symmetry is inclined by $\sim$50° with respect to the line of sight (RLoS),

• a southern lobe approaching to us with an inclination angle $\sim$40° (RLoS) and polar expansion $\simeq$60 km s^{-1}, and

• two northern lobes with inclination angles $\sim$115° and $\sim$127° receding from us with polar expansion velocities $\simeq$77 and $\simeq$84 km s^{-1}, respectively.

In this way, the physical structure of NGC 6369 is reminiscent of other barrel-shaped PNe with polar extensions that result in a spindle shape (e.g., NGC 3918, Corradi et al. 1999).

According to this model and for the distance of 1,550 pc proposed by Monteiro et al. (2004), the kinematical ages of the barrel and bipolar lobes are $\simeq$2,000 yrs and $\simeq$3,200 yrs, respectively. The kinematical age of the inner shell is thus smaller than that of the bipolar lobes, most likely indicating important dynamical effects that have made the kinematical and real ages to differ. These dynamical effects may also be revealed by the distorted eastern structure whose complex shape would arise from the interaction of an expanding, regular lobe with extended and irregular material along its direction. Alternatively, this bifurcated structure may arise from intrinsic multipolar collimated outflows as has been claimed in other PNe (Manchado, Stanghellini, & Guerrero 1996; Sahai 2000).

5.2 Kinematics of the envelope

The emission from the outer envelope of NGC 6369 is registered by the slits at positions #1, #3, #4, and #5, although the echellograms at positions #3 and #4 only cover a small fraction of this shell. In the echellograms at positions #1 and #5, the Hα and [N II] lines are extremely narrow, with FWHM $\simeq$ 32 km s^{-1} and $\simeq$ 20 km s^{-1}, respectively. We note, however, that the velocity centroid along these lines is not constant: the echellogram at position #1 shows a weavy pattern (best seen in the [N II] line), whereas at position #5 displays an arc-like shape. We measure velocity differences up to 17 km s^{-1}. We also note that emission is patchy, especially in the [N II] line.

Clearly the envelope is not inert, but the narrow and weavy/arced line shape does not comply with the expectations for an expanding shell, even if it had the low expansion velocity (Meaburn et al. 1996; Guerrero, Villaver, & Manchado 1998) presumed for the slow AGB wind. The knotty and fragmented appearance of the envelope of NGC 6369 indicate that the kinematics revealed by the echellograms is governed by the emission from individual knots, rather than by the emission from a continuous shell. This situation is reminiscent of many other PNe where bright low-ionization knots are embedded within a faint envelope around a bright inner shell, e.g., NGC 2392 and NGC 7354 (O'Dell et al. 2002; Contreras et al. 2010). As for these two PNe, the relatively low velocity differences measured for the knots of the envelope of NGC 6369 would suggest that they lay at different latitudes with respect to the symmetry axis of the barrel, but mostly on a weavy disk-like or flattened structure, as for NGC 2392 and NGC 7354.

5.3 Extension of the photo-dissociation region

The relative sizes of the regions dominated by ionized material and molecules and dust are illustrated in Figure 12 that displays the normalized surface brightness profiles in the *HST* Hα and [N II], WHT LIRIS H_2, and *Spitzer* IRAC 4.5 and 8.0 μm images. The comparison between these profiles confirms that the surface brightness profiles of the inner shell of NGC 6369 of the optical Hα emission line and mid-IR IRAC 4.5 and 8.0 μm bands are very similar in shape and extent. The mid-IR and optical profiles start to depart from each other at the edge of the inner shell: the emission from Hα and [N II] drops considerably in an annular region between 20″ and 25″ (i.e., the inner regions of the envelope), while the emission in the IRAC 4.5 and 8.0 μm bands stays higher and the H_2 profile shows increased emission. On the contrary, on the 25″–35″ outer rim of the envelope, the emission in the Hα and [N II] lines is enhanced, while the emission in the IRAC 4.5 and 8.0 μm bands flattens and then decays smoothly. There is no H_2 emission in this range of radial distances.

The comparison of the relative shapes and extents of these different surface brightness profiles is relevant to the understanding of the physical structure of NGC 6369. Its inner shell is mostly ionized and thus the emission in the IRAC 4.5 and 8.0 μm bands is dominated by ionic emission. The shell is enclosed by a series of "tadpole" or "cometary" knots whose prominent low-excitation [N II] and molecular H_2 emission at their heads result in bright [N II] and H_2 peaks at $\simeq$13″. The inner shell is surrounded by a region dominated by molecular material, the inner rim of the envelope between $\sim$17″ and $\sim$25″. This region, outside the bright inner shell and beyond the annular region defined by the tails of the "cometary" knots, seems to be a real PDR. The relative brightening of the emission in the IRAC 4.5 and 8.0 μm bands at these radial distances is very

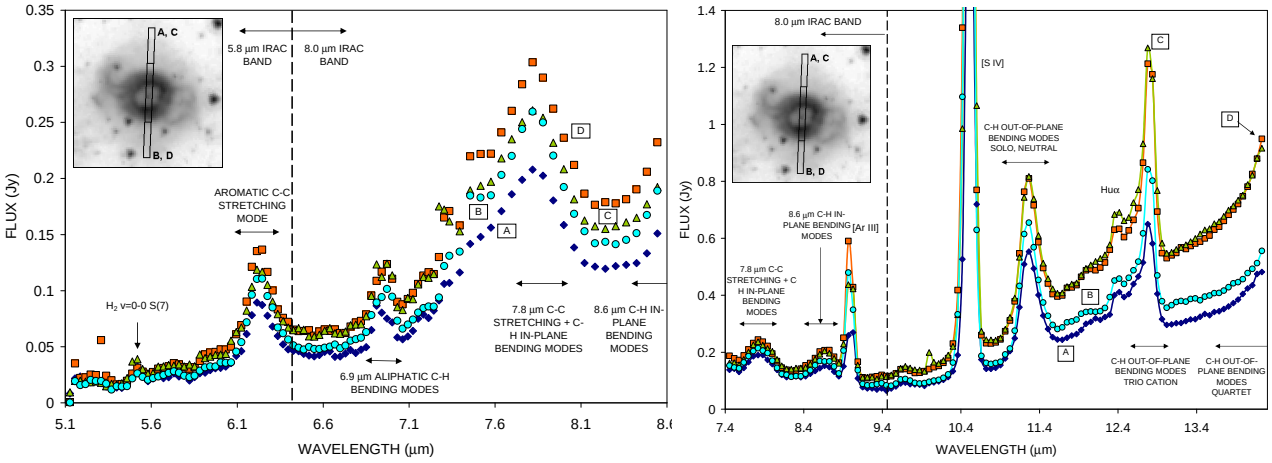

Figure 9. *Spitzer* IRS spectrum of NGC 6369 in the SL2 short (*left*) and SL1 long (*right*) wavelength ranges taken at the four overlapping positions shown in the inset: A (dark blue diamonds), B (cyan open dots), C (green triangles), and D (red squares). Positions A and C cover the inner shell and north portion of the envelope, whereas positions B and D also cover the inner shell, but the south portion of the envelope. Despite the (symmetric) displacement between positions B+D and A+C, the spectra are mostly consistent. The spectral range $\sim$ 7.3–7.6 μm corresponds at two overlapping spectral sequences, and results in this regime should be considered as unreliable.

likely due to molecular H_2 emission, although a contribution from continuum dust or PAH emissions is also very likely as noted in other PNe (e.g., Phillips & Ramos-Larios 2008, 2010; Ramos-Larios & Phillips 2008). Finally, the outer rim of the envelope is again dominated by ionic emission, but we note that low-excitation emission dominates. This may explain the flattening of the emission in the IRAC 4.5 and 8.0 μm emission due to an additional contribution of ionic emission.

It is finally worth noting that sources with comparable He II and H I Zanstra temperatures are likely to be ionisation bound and enveloped by a shell of neutral material. This leads to a correlation between the Zanstra ratio T_Z(He II)/T_Z(H I), and mid-IR extent outside of the ionised shell (see e.g., Quino-Mendoza, Phillips, & Ramos-Larios 2011). NGC 6369 seems to be a peculiar case of this correlation: whereas the emission from molecular material causes a larger dimension of its inner shell at mid-IR wavelenghts, the presence of ionized material in its singular envelope results in very similar final optical and mid-IR dimensions.

5.4 Shock excitation?

In §3.1 we noted the large jump in the [N II] to [O III] ratio at the filamentary structures that enclose the eastern and western extensions of the inner shell of NGC 6369. Given that these structures are at the tips of bubble-like structures that may arise from bipolar outflows, it is very likely that the unusually high [N II]/[O III] ratios stem from shock interactions of these structures with surrounding material. To investigate the structure of these features in more detail, we show in Figure 13 a radial profile across a particularly bright filament of the eastern extension extracted from the *HST* Hα, [N II], and [O III] images and ratio maps.

The comparison of the surface brightness profiles indicates that the peak of all these three emission lines are almost coincident, but the spatial profile of the [O III] line is noticeable broader. The inner shoulder of this profile, closer to the central star (negative offsets in Fig. 13), can be explained as the result of a higher photo-excitation. The shoulder of the line farther away from the nebula, however, cannot be explained in this way and it very likely reveals the presence of a forward shock propagating onto a lower density medium. The [O III]/Hα ratio profile in the lower-panel of Fig. 13 allows us to derive a quantitative value for the spatial extent of this post-shock region, $\simeq 1\farcs2$. At the distance of 1,550 pc, this corresponds to $\sim 3\times10^{16}$ cm, comparable to the post-shock cooling widths determined from modelling of shocks (e.g., Dopita 1977; Shull & McKee 1979; Pittard et al. 2005).

5.5 The external condensations of NGC 6369

There is a growing number of PNe in the literature that show knots or blobs of emission well separated from their main nebular shells that do not form a halo. In some cases, the kinematics of these knots imply high-velocity collimated outflows, e.g., Fleming 1 (Palmer et al. 1996) or MyCn 18 (Redman et al. 2000), while in some others, e.g., IC 4634 (Guerrero et al. 2008), the velocity of the knots is close to the systemic velocity, may be due to motions close to the plane of the sky.

As for NGC 6369, we note that one of the blobs located outside its inner shell and envelope is detected in the Hα and [N II] emission lines at the slit position #1 (Fig. 4). This blob, at an offset of $\sim$70$''$ from NGC 6369 central star, has a relatively small velocity shift, $\sim$+17 km s^{-1}, with respect to the systemic velocity, and its velocity width is small, FWHM $\simeq$ 26 km s^{-1} in Hα and $\simeq$ 21 km s^{-1} in [N II].

The kinematical properties of this outer condensation make NGC 6369 closer to the case of the lower velocity knots of IC 4634 than to a case of high-velocity collimated outflows. Meanwhile, the velocity shift, although small, would preclude that these outer condensations are part of an incomplete halo (as, e.g., the case of IC 4593, Corradi et al. 1997). The origin of these external condensations is uncer-

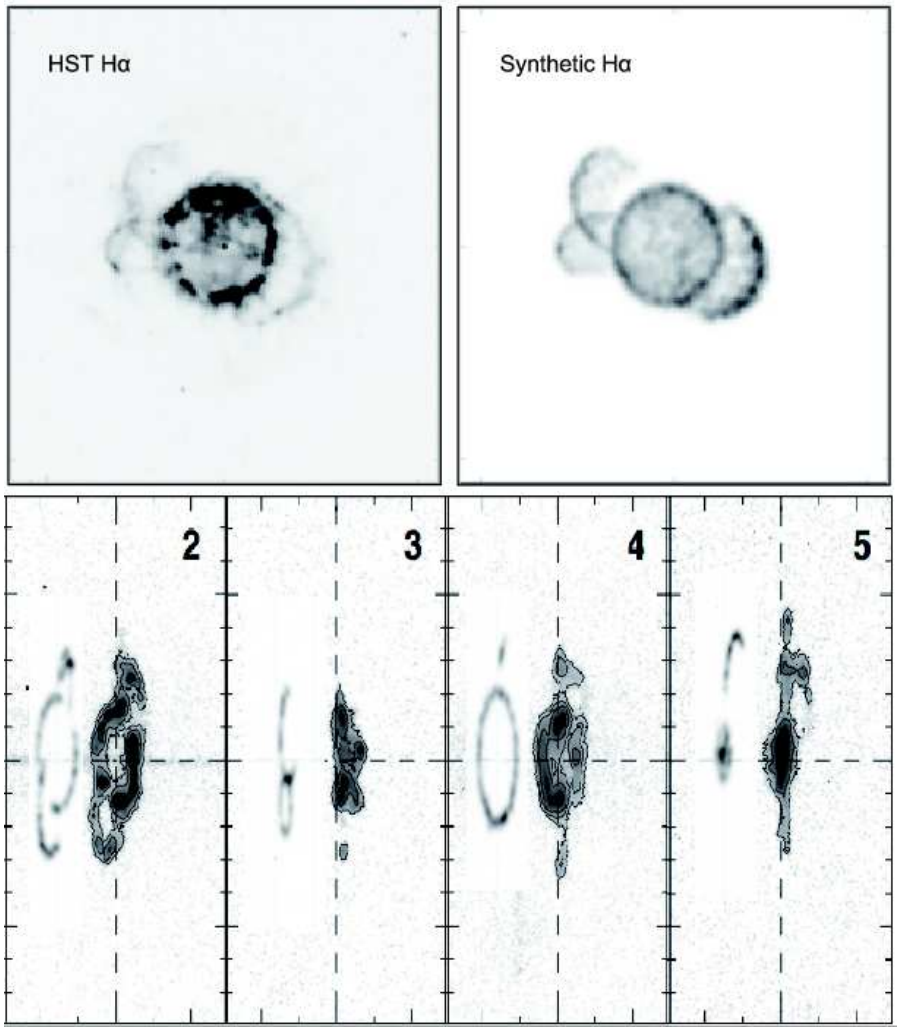

Figure 10. (*top*) *HST* Hα (*left*) and synthetic Hα (*right*) images of NGC 6369. (*bottom*) PV maps from the model compared to the observed PV maps. The synthetic PV maps have been displaced towards higher velocities (to the left in the PV maps) to allow a fair comparison.

tain, but they may probe earlier, point-symmetric ejections, or arise from shocks associated with the east-west that excite material surrounding the nebula.

5.6 Physical structure of NGC 6369

The spatio-kinematical model of the inner shell of NGC 6369, the kinematics of its envelope, and the intrincate distributions of ionized, molecular, and mid-IR emission can be used to obtain a coherent view of its structure. The inner shell and extensions of NGC 6369 can be described as a tilted equatorial barrel with bipolar extensions.

This inner shell is encircled by a ring of [N II]-bright "cometary" knots. The envelope is formed by an ensemble of discrete low-ionization and molecular blobs and knots probably embedded within a much fainter, fully ionized shell. These knots seem to be distributed at slightly different latitudes with respect to the barrel symmetry axis, but mostly on a weavy disk-like or flattened structure.

Near- and mid-IR H_2 emission encompasses the inner shell, revealing a real PDR that seems to be inside the envelope, a shell of ionized gas. It is unclear whether this PDR exists within the envelope, or whether this is a projection

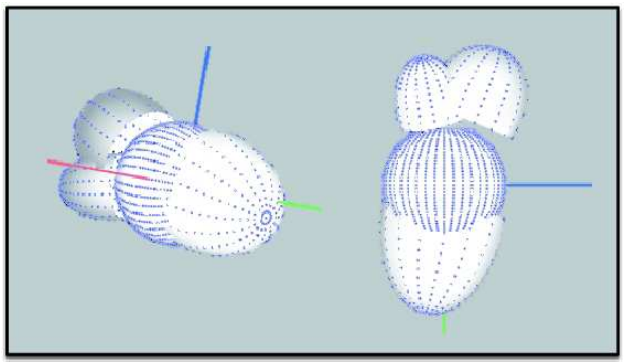

Figure 11. Main structures of NGC 6369 represented in a 3D model. The left panel corresponds to the inclination and PA proposed. The right panel is the same structure but rotated to show a complementary view of the model.

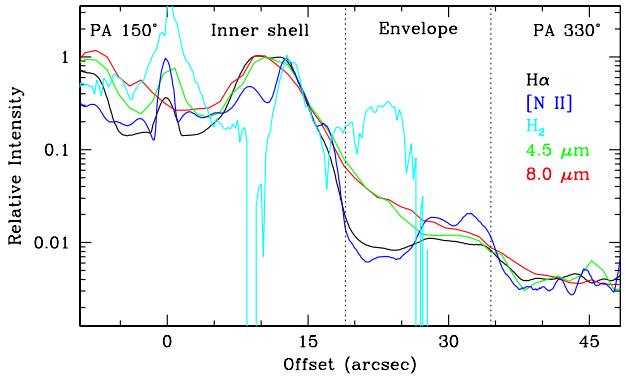

Figure 12. Surface brightness profiles of the Hα (black), [N II] (blue), WHT H_2 (cyan), IRAC 4.5 μm (green), and IRAC 8.0 μm (red) along PA 330° through the central star of NGC 6369. The profiles have been normalized to the emission peak at the bright inner shell. The location of the inner shell end envelope edges are marked by vertical dotted lines.

effect, so that the PDR is located at high nebular latitudes, above and below the envelope that would be a rather flat structure only present at low latitudes.

6 CONCLUSIONS

Using narrow-band optical and near-IR images, broad-band mid-IR images, optical long-slit echelle spectra and mid-IR spectra, we have investigated the physical structure of the planetary nebula NGC 6369. The inner shell and its east-west extensions can be modeled in terms of a tilted barrel of ionized gas and bipolar outflows at its tips, in broad agreement with previous observations of the source. The nebula is optically thick to H ionizing radiation, thus allowing the existence of a PDR that is confirmed by its H_2 emission and suggested by an additional contribution of dust continuum and PAH band emission to the IRAC images in the 5.8 and 8 μm bands. The envelope does not seem to be a real shell enclosing the inner shell, but rather a flattened structure at the equatorial regions of NGC 6369. Molecular and low-excitation emission of [N II] is also detected in small irregular condensations well outside the main nebular shells. Finally, we note that *HST* images show the presence of "cometary" knots at the rim of the inner shell whose appearance is similar to those of features in NGC 2392 and NGC 7354, among other PNe.

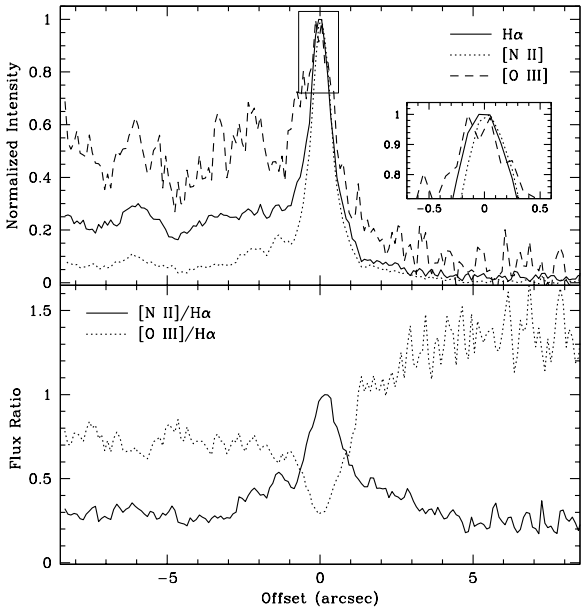

Figure 13. (*top*) [N II], Hα, and [O III] surface brightness profiles through a likely shock structure in the eastern extension of the inner shell of NGC 6369. Negative offsets are closer to the central star, while positive offsets corresponds to regions farther away from the main nebula. (*bottom*) [N II]/Hα and [O III]/Hα ratio profiles.

ACKNOWLEDGMENTS

GRL acknowledges support from CONACyT and PROMEP (Mexico). MAG and GRL are partially funded by grant AYA2008-01934 of the Spanish Ministerio de Ciencia e Innovación (MICINN). RV, MAG and GRL thank support by grant IN109509 (PAPIIT-DGAPA-UNAM). We also would like to thank to the referee R. Corradi who made very excellent comments for the improvement of the paper.

Based on observations made with the Observatorio Astronómico Nacional at the Sierra de San Pedro Mártir, OAN-SPM, wich is operated by the Instituto de Astronomía of the Universidad Nacional Autónoma de México.

The William Herschel Telescope is operated on the island of La Palma by the Isaac Newton Group in the Spanish Observatorio del Roque de los Muchachos of the Instituto de Astrofísica de Canarias.

Based on observations made with the Nordic Optical Telescope, operated on the island of La Palma jointly by Denmark, Finland, Iceland, Norway, and Sweden, in the Spanish Observatorio del Roque de los Muchachos of the Instituto de Astrofísica de Canarias.

This research has made use of the NASA/ IPAC Infrared Science Archive, which is operated by the Jet Propulsion Laboratory, California Institute of Technology, under contract with the National Aeronautics and Space Administration.

We would like to dedicate this paper in memory of our colleague and friend, Prof. John Peter Phillips, who recently passed away.

REFERENCES

Acosta Pulido J. A., et al., 2003, INGN, 7, 15
Aller L.H., & Keyes C.D., 1987, ApJS, 65, 405
Bernard Salas J., Pottasch S. R., Beintema D. A., Wesselius P. R., 2001, A&A, 367, 949
Cohen M., & Barlow M. J., 2005, MNRAS, 362, 1199
Contreras M. E., Vázquez R., Miranda L. F., Olguín L., Zavala S., & Ayala S., 2010, AJ, 139, 1426
Corradi R. L. M., Guerrero M., Manchado A., Mampaso A., 1997, NewA, 2, 461

Corradi, R. L. M., Perinotto, M., Villaver, E., Mampaso, A., & Gonçalves, D. R. 1999, ApJ, 523, 721
Corradi R. L. M., 2004, ASPC, 313, 148
de Graauw T., et al., 1996, A&A, 315, L49
Dopita M.A., 1977, ApJS, 33, 437
Fazio G., et al., 2004, ApJS, 154, 10
Guerrero M. A., Manchado A., & Serra-Ricart M., 1996, ApJ, 456, 651
Guerrero M. A., Villaver E., & Manchado A., 1998, ApJ, 507, 889
Guerrero M. A., et al., 2008, ApJ, 683, 272
Hajian A. R., Balick B., Terzian Y., & Perinotto M., 1997, ApJ, 487, 304
Hony S., Waters L. B. F. M., & Tielens A. G. G. M., 2001, A&A, 378, L41
Houck J.R., et al., 2004, ApJS, 154, 18
Hrivnak B. J., Volk K., & Kwok S., 2009, ApJ, 694, 1147
Kwok S., Volk K., & Hrivnak B. J., 1999, IAUS, 191, 297
Li A., & Draine B.T., 2001, ApJ, 554, 778
Manchado A., Stanghellini L., & Guerrero M.A., 1996, ApJ, 466, L95
Meaburn J., López J. A., Bryce M., & Mellema G., 1996, A&A, 307, 579
Meaburn J., López J. A., Gutiérrez L., Quiróz F., Murillo J. M., Valdez J., Pedrayez M., 2003, RMxAA, 39, 185
Monteiro H., Schwarz H.E., Gruenwald R., & Heathcote S., 2004, ApJ, 609, 194
O'Dell C. R., Balick B., Hajian A. R., Henney W. J., Burkert A., 2002, AJ, 123, 3329
O'Dell C. R., Weiner L. D., & Chu Y.-H., 1990, ApJ, 362, 226
Palmer J. W., López J. A., Meaburn J., & Lloyd H. M., 1996, A&A, 307, 225
Phillips J. P., 2003, MNRAS, 344, 501
Phillips J.P., & Ramos-Larios G., 2008, MNRAS, 383, 1029
Phillips J.P., Ramos-Larios G., 2010, MNRAS, 405, 2179
Pittard J.M., Dobson M.S., Durisen R.H., Dyson J.E., Hartquist T.W., & O'Brien J.T., 2005, A&A, 438, 11
Pottasch S.R., & Bernard-Salas J., 2008, A&A, 490, 715
Quino-Mendoza J.A., Phillips J.P., Ramos-Larios G., 2011, RMA&A, 47, 31
Ramos-Larios G., & Phillips J.P., 2008, MNRAS, 390, 1014
Redman M. P., O'Connor J. A., Holloway A. J., Bryce M., & Meaburn J., 2000, MNRAS, 312, L23
Sabbadin F., Cappellero E., Benetti S., Turatto M., & Zanin C. 2000, A&A, 355, 688
Sahai R., 2000, ApJ, 537, L43
Schneider S.E., Terzian Y., Purgathofer A., & Perinotto M., 1983, ApJS, 52, 399
Schwarz H. E., Corradi R. L. M., Melnick J., 1992, A&AS, 96, 23
Shull J.M., & McKee C.F., 1979, ApJ 227, 131
Solf J., & Ulrich H., 1985, A&A, 148, 274
Steffen, W., Koning, N., Wenger, S., Morisset, C., & Magnor, M. 2011, IEEE Transactions on Visualization and Computer Graphics, 17, 454
Steffen W., & López J.A., 2006, RMA&A, 42, 99
Van Winckel H., & Reyniers M., 2000, A&A, 354, 135
Zhang K., Jiang B. W., & Li A., 2009, MNRAS, 396, 1247
Zuckerman B., & Aller L.H., 1986, ApJ, 301, 772

This paper has been typeset from a TEX/ LATEX file prepared by the author.